Realization of an Adaptive Radiative Cooler with a Multilayer-Filter VO_2-Based Fabry–Pérot Cavity

Hengli Xie(谢恒立), Huaiyuan Yin(殷怀远), and Chunzhen Fan(范春珍)*

School of Physics and Laboratory of Zhongyuan Light, Zhengzhou University, Zhengzhou 450001, China

(Received 30 January 2024; accepted manuscript online 12 March 2024)

A high-performance adaptive radiative cooler comprising a multilayer-filter VO_2-based Fabry–Pérot (FP) cavity is proposed. The bottom FP cavity has four layers, VO_2/NaCl/PVC/Ag. Based on the phase transition of VO_2, the average emissivity in the transparent window can be switched from 3.7% to 96.3%. Additionally, the average emissivity can also be adjusted with external strain to the PVC layer, providing another way to attain the desired cooling effect. An upper filter is included to block most of the solar radiation and provide a transmittance of 96.7% in the atmospheric window. At high temperature, the adaptive emitter automatically activates radiative cooling. The net cooling power is up to 156.4 $W\cdot m^{-2}$ at an ambient temperature of 303 K. Our adaptive emitter still exhibits stable selective emissivity at different incident angles and heat transfer coefficients. At low temperature, the radiative cooling automatically deactivates, and the average emissivity decreases to only 3.8%. Therefore, our work not only provides new insights into the design of high-performance adaptive radiative coolers but also advances the development of intelligent thermal management.

DOI: 10.1088/0256-307X/41/4/044202

Radiative cooling is a passive cooling technology that radiates heat from hot objects into cold outer space through the atmospheric transparent window.[1,2] To enable daytime radiative cooling, near-zero solar energy absorption and ultra-high long-wave infrared (LWIR) emission are required. In recent years, the utilization of photonic crystals,[3–6] random particles,[7–9] porous films[10–12] and metamaterials[13–17] has been demonstrated to achieve effective radiative cooling. However, these static radiative coolers are only effective in high temperatures and are not suitable for low-temperature environments. Therefore, it is necessary to develop an adaptive radiative cooler with temperature-responsive features.

An adaptive radiative cooler should have the ability to autonomously switch cooling on or off as the environmental temperature varies. It should display large solar reflectance and high infrared emissivity for cooling at high temperature and small infrared emissivity at low temperature to avoid heat loss.[18] However, such a dynamic spectral response is difficult to realize in only one device. One possible solution is the utilization of external stimuli such as electrical, mechanical and wetting to trigger cooling or heating.[19–21] For example, Zhang *et al.* fabricated infrared electrochromic devices by assembling polyaniline porous membranes doped with perchloric acid. An emissivity modulation of 0.316–0.735 was achieved in the wavelength range from 2.5 μm to 25 μm.[19] Xia *et al.* added a louver structure above a static radiative cooler with memory springs to adjust the blade opening angle, thereby controlling the on/off of the cooling.[20] Mandal *et al.* proposed a porous polymer coating, the transmittance which changes upon reversible wetting with ordinary liquids, allowing for 3.2 ℃ of cooling and 21.4 ℃ of solar heating.[21] Nevertheless, dynamic switching of these structures requires additional stimuli or complex mechanical systems, which limits their large-scale application.

Recently, the use of phase change materials has proven to be more advantageous for implementing adaptive radiative cooling. Among them, vanadium dioxide (VO_2) is a typical phase transition material, and its dielectric constants present a large difference in LWIR before and after phase transition.[22] Moreover, the phase transition process is reversible with a response time close to a femtosecond.[23] Currently, VO_2-based adaptive radiative coolers have attracted much attention.[24–27] For instance, Ono *et al.* constructed a radiative cooler consisting of VO_2/MgF_2/W with a spectrally selective filter consisting of Ge and MgF_2. The emissivity tuning range was from 5.4% to 63.6%.[28] Tang *et al.* decreased the phase transition temperature of VO_2 nanoparticles to near room temperature by doping with W. They developed a temperature-adaptive radiative coating, which allows for 20% to 90% modulation of infrared emissivity and 20% solar energy absorption through a metal–insulator transition.[29] Xie *et al.* constructed a thin film composed of switchable resonators and Bragg reflectors, realizing solar absorption of 0.121 and emissivity tunability of 0.825.[30] Liang *et al.* designed a VO_2/Ge/VO_2/Ag multilayer structure and achieved an emissivity of 0.78 in the metallic state and close to 0.10 in the dielectric state.[31] Li *et al.* proposed an adaptive radiative cooling system based on W–VO_2, which enabled a high modulation rate of 0.909 in the atmospheric window.[32] Huang *et al.* doped VO_2-based core-shell nanoparticles in a polyethy-

*Corresponding author. Email: chunzhen@zzu.edu.cn

© 2024 Chinese Physical Society and IOP Publishing Ltd

lene matrix to prepare a radiative cooling film with adaptive capability. The maximum cooling power variation of the films was 61.7 $W \cdot m^{-2}$.[33] Bhupathi *et al.* prepared VO_2/ZnSe/ITO/glass thin films with porous VO_2 microstructures, obtaining emissivity tunability of more than 0.4 in the LWIR band.[34] Although previous works have demonstrated that adaptive radiative cooling is achievable based on VO_2, the low atmospheric transmittance of the top filter hinders the thermal radiation from the bottom cooler. Furthermore, the high emissivity present in the adaptive radiative emitter at low temperature will inevitably lead to heat loss. Therefore, there is an urgent demand for the development of high-performance adaptive radiative coolers to accelerate their application.

In this work, we design an adaptive radiative cooling emitter that can automatically activate or deactivate the cooling function depending on the ambient temperature. Firstly, we investigate a VO_2-based FP radiative cooler to achieve an average emissivity modulation from 3.8% to 96.3% within the atmospheric window. It can be well explained by FP resonance. Additionally, the thickness of the dielectric layer of PVC can be tuned with strain, allowing for further control over the emissivity. We then employ a multilayer filter composed of Si and KBr layers to isolate the interference from solar radiation. The combination of the filter and FP cavity constitutes an adaptive radiative cooling emitter. It exhibits an ultra-high transmittance of 96.7% in the atmospheric window and a low transmittance of 2.5% in the solar spectrum. Notably, the cooling performance still exists at different incident angles and heat transfer coefficients. Therefore, our research provides a new approach for obtaining smart thermal management.

Design. The structure of our adaptive radiative cooler is shown in Fig. 1(a). It consists of a filter (upper) and an FP cavity (lower). The gap distance D is much larger than the incident wavelength λ. The filter is composed of alternating Si and KBr layers to isolate the interference from sunlight and maintain high transmission in the atmospheric window. The bottom FP cavity is employed to achieve on/off switching of the cooling; it has a multilayer structure of VO_2, NaCl, PVC and Ag from top to bottom with thicknesses $d_1 = 15\,\text{nm}$, $d_2 = 900\,\text{nm}$, and $d_3 = 1000\,\text{nm}$, respectively. The optical parameters of the materials are taken from Ref. [35]. NaCl and PVC, which exhibit very low extinction coefficients in transparent windows, are used for the interlayer materials.

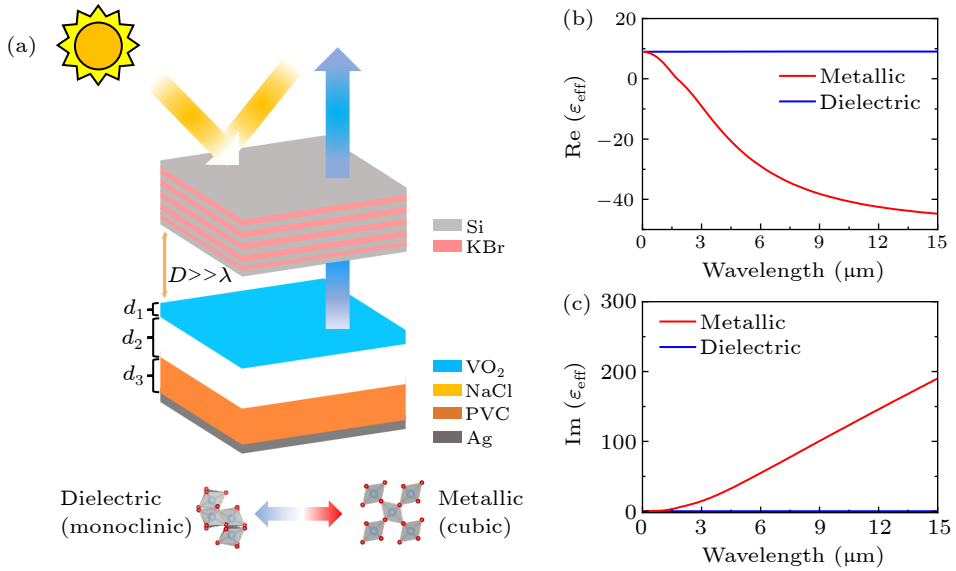

Fig. 1. (a) The designed adaptive radiative cooler consists of a multilayer filter (upper) and an FP cavity (lower). The top layer consists of alternating Si and KBr layers. The bottom layer is VO_2/NaCl/PVC/ Ag. The thicknesses are $d_1 = 15\,\text{nm}$, $d_2 = 900\,\text{nm}$, and $d_3 = 1000\,\text{nm}$. The real (b) and imaginary parts (c) of the VO_2 dielectric constant in the range from 0 to 15 μm.

The phase transition of VO_2 is strongly dependent on its critical temperature. The dielectric phase transits to a metallic phase when the external temperature exceeds the transition temperature. The effective dielectric constants can be described using the effective medium theory as follows:[36]

$$\varepsilon_{\text{eff}} = \frac{1}{4}\Big\{\varepsilon_{\text{i}}(2-3f) + \varepsilon_{\text{m}}(3f-1) \pm \sqrt{[\varepsilon_{\text{i}}(2-3f) + \varepsilon_{\text{m}}(3f-1)]^2 + 8\varepsilon_{\text{i}}\varepsilon_{\text{m}}}\Big\}. \quad (1)$$

Here, ε_{i} is the dielectric constant in the dielectric phase of VO_2; f represents the volume fraction upon the temperature, which can be expressed as[37]

$$f = 1 - \frac{1}{1+\exp\left[(T-T_{\text{c}})/\Delta T\right]}, \quad (2)$$

where T denotes the temperature of the VO_2 surface, T_{c} is the phase transition temperature, taken as 298 K, and $\Delta T = 6\,\text{K}$ is the hysteresis temperature.[22] The doping of W in VO_2 can reduce the phase transition temperature without significantly affecting its complex refractive index.[27,31] The dielectric constant of metallic phase VO_2

can be solved according to the Drude model[38]

$$\varepsilon_{\mathrm{m}} = 9 - \frac{\omega_{\mathrm{p}}^2}{\omega\left(\omega + i\tau^{-1}\right)}. \tag{3}$$

The plasma frequency $\omega_{\mathrm{p}} = \sqrt{Ne^2/\varepsilon_0 m^*}$ and $N = 8.75 \times 10^{27}\,\mathrm{m}^{-3}$ is the carrier concentration. The effective mass $m^* = 2m_{\mathrm{e}}$, where m_{e} is the mass of a free electron. The relaxation time $\tau = \mu m^*/e$, where $\mu = 2\,\mathrm{cm}^2{\cdot}\mathrm{V}^{-1}{\cdot}\mathrm{s}^{-1}$.[39,40]

The effective dielectric constant of VO_2 in the dielectric and metallic phases can be solved by combining Eqs. (1)–(3). The real and imaginary parts of the effective dielectric constant of VO_2 are shown in Figs. 1(b) and 1(c). It can be clearly observed that the real part $[\mathrm{Re}\,(\varepsilon_{\mathrm{eff}})]$ of VO_2 is positive and the imaginary part $[\mathrm{Im}\,(\varepsilon_{\mathrm{eff}})]$ is nearly zero when VO_2 is in the dielectric phase. Namely, it behaves as a dielectric layer at low temperature. However, when VO_2 is in the metallic phase at high temperature, the real part becomes negative and the imaginary part is frequency dependent, exhibiting high absorption in the LWIR band. Therefore, VO_2 can switch from the dielectric phase to the metallic phase upon change in the external temperature.

Our numerical calculations are carried out with COMSOL Multiphysics based on the finite element method.[41] To model the design and to simplify the calculation process, we establish a unit cell and simulate an infinite array with periodic boundary conditions. Unphysical reflections at the upper and lower boundaries are eliminated by adding perfectly matched layers. We have chosen tetrahedral and triangular meshes with a minimum size of 13 nm. Due to the small thickness of the VO_2 layer (only 15 nm), the transition boundary conditions are used to improve the accuracy of the simulation results and avoid abrupt changes or discontinuities in the meshing. The incident electromagnetic waves are along the z-direction and the default electric field polarization is along the x-direction. Finally, the emissivity is calculated using the equation $\varepsilon = 1 - R - T$, where reflectance $R = |S_{11}|^2$ and transmittance $T = |S_{21}|^2$. With the rapid advancement of fabrication techniques, it is now feasible to implement our proposed adaptive radiative cooler in the lab. The proposed procedures is follows. Firstly, a Ag layer with thickness of 200 nm is deposited on a quartz glass surface using direct current magnetron sputtering.[42] Next, a PVC layer is constructed with the calendaring method. Then, NaCl film and VO_2 film are deposited sequentially by molecular beam epitaxy.[43,44] Additionally, the upper multilayer filter can be achieved through magnetron sputtering.[42]

Radiative Cooling Power. The cooling performance of our adaptive radiative cooler can be assessed from the net radiative cooling power P_{net}.[4,45] The energy exchange consists of four parts: the absorbed solar energy P_{sun}, the atmospheric energy P_{atm}, the convection power P_{nonrad}, and the surface emission power P_{rad}. P_{net} can be written as

$$P_{\mathrm{net}}(T) = P_{\mathrm{rad}}(T) - P_{\mathrm{atm}}(T_{\mathrm{amb}}) - P_{\mathrm{sun}} - P_{\mathrm{nonrad}}(T, T_{\mathrm{amb}}). \tag{4}$$

Here, P_{rad} is the power radiated from the structure,

$$P_{\mathrm{rad}}(T) = 2\pi A \int_0^{\pi/2} d\theta \sin\theta\cos\theta \times \int_0^{\infty} d\lambda I_{\mathrm{BB}}(T, \lambda)\,\varepsilon(\lambda, \theta), \tag{5}$$

where A is the surface area of the radiative cooler, T is the temperature of the cooler surface, and $\varepsilon(\lambda, \theta)$ denotes the spectral emissivity of the radiator. The black-body thermal radiation $I_{\mathrm{BB}}(T, \lambda)$ can be expressed as

$$I_{\mathrm{BB}}(T, \lambda) = \frac{2hc^2}{\lambda^5}\frac{1}{e^{\frac{hc}{\lambda k_{\mathrm{B}} T}} - 1}, \tag{6}$$

where h is Planck's constant, k_{B} is Boltzmann's constant, c is the speed of light in vacuum, and λ is the wavelength.

The atmospheric thermal radiation power P_{atm} is written as

$$P_{\mathrm{atm}}(T_{\mathrm{amb}}) = 2\pi A \int_0^{\pi/2} d\theta \sin\theta\cos\theta \int_0^{\infty} d\lambda I_{\mathrm{BB}}(T_{\mathrm{amb}}, \lambda) \times \varepsilon(\lambda, \theta)\,\varepsilon_{\mathrm{atm}}(\lambda, \theta), \tag{7}$$

where T_{amb} is the ambient temperature, taken to be 300 K in this work. The integration range of λ is from 8 to 13 μm. The atmospheric emissivity is given by $\varepsilon_{\mathrm{atm}}(\lambda, \theta) = 1 - t(\lambda)^{1/\cos}$, with $t(\lambda)$ being the atmospheric transmittance in the zenith direction.[46]

P_{sun} is the solar energy absorbed by the radiative cooler

$$P_{\mathrm{sun}} = A \int_0^{\infty} d\lambda \varepsilon(\lambda, \theta_{\mathrm{sun}})\, I_{\mathrm{AM1.5}}(\lambda), \tag{8}$$

where $I_{\mathrm{AM1.5}}(\lambda)$ is the solar irradiance of the AM1.5 spectrum, here taken as $1000\,\mathrm{W}{\cdot}\mathrm{m}^{-2}$.[47]

The heat loss under non-radiative conditions is written as[48–50]

$$P_{\mathrm{nonrad}}(T, T_{\mathrm{amb}}) = Ah_{\mathrm{c}}(T_{\mathrm{amb}} - T), \tag{9}$$

where h_{c} is the nonradiative heat transfer coefficient. It can be evaluated by measuring wind speed and is expressed as $h_{\mathrm{c}} = 1.44v + 4.955$, with v being the wind speed. In the outdoor environment, because the wind speed is generally moderate, it is taken as 0–5 $\mathrm{m}{\cdot}\mathrm{s}^{-1}$.[51] Thus, the value of h_{c} is usually taken from 6 to 10 $\mathrm{W}{\cdot}\mathrm{m}^{-2}{\cdot}\mathrm{K}^{-1}$.

The average emissivity $\bar{\varepsilon}$ in the atmospheric window can be represented as

$$\bar{\varepsilon}_{8-13\,\mu\mathrm{m}} = \frac{\int_8^{13} \varepsilon(\lambda, \theta)\, I_{\mathrm{BB}}(T, \lambda)\, d\lambda}{\int_8^{13} I_{\mathrm{BB}}(T, \lambda)\, d\lambda}. \tag{10}$$

Results and Discussion. We first investigate the emissivity of the radiative cooler from 3 μm to 15 μm without the top filter in Fig. 2(a). Ultra-high selective emission is observed in the atmospheric transparency window when VO_2 is in the metallic phase. Specifically, the average emissivity is as high as 96.3%, ensuring an efficient and continuous cooling performance. However, the emission curve is almost flat in the dielectric phase, and its average emissivity reduces to 3.8%, which prevents heat dissipation. Therefore, the adaptive optical response can

be well regulated with the external temperature. Moreover, we also calculated the emissivity of NaCl at different thicknesses and found that the average emissivity is maximum when the thickness is taken as 9 μm. The physical mechanism of the radiative cooler can be explained by the FP resonance in Figs. 2(b) and 2(c).[28,52] Four constituent layers form a resonant cavity when VO_2 is in the metallic state. Electromagnetic waves propagate in the structure undergoing multiple reflection and transmission, and a strong resonance phenomenon occurs at 3.70 μm and 9.89 μm. The resonant cavity does not exist when VO_2 is in the dielectric state. Thereby, the incoming electromagnetic waves propagate through the top layer of VO_2 and the low emissivity is mainly due to the absorption of the dielectric PVC layer. It is worth mentioning that modulation of the emissivity spectrum can be achieved if a PVC or NaCl layer is used separately as an intermediate layer, but the reflection and emissivity are not as high as that for a NaCl/PVC layer. In addition, the Ag layer can be replaced by an Al layer, and efficient adaptive radiative cooling can still be achieved. Here we take Ag as the substrate layer due to its stability in air in practical applications.

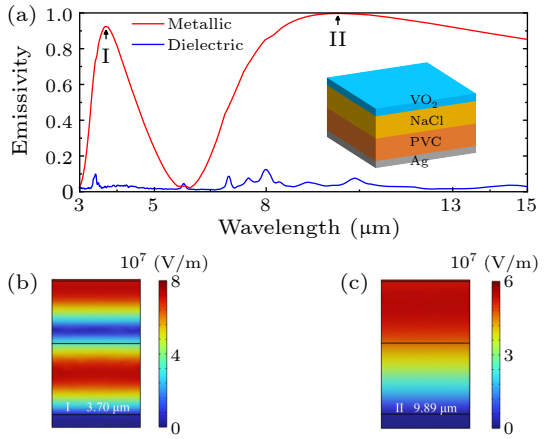

Fig. 2. (a) Emissivity of the VO_2-based radiative cooler in metallic and dielectric states. [(b), (c)] electric field distributions at resonance positions. Here $\lambda = 3.70$ μm and 9.89 μm when VO_2 is in the metallic state.

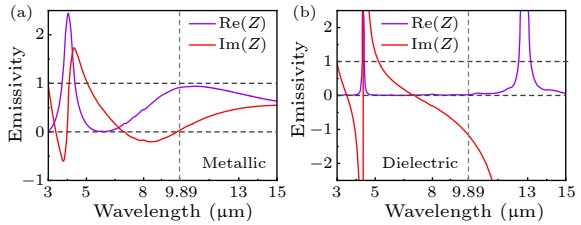

Fig. 3. Real and imaginary parts of the equivalent impedance of the adaptive radiative cooler in the infrared band.

In addition, the equivalent impedance Z of the multilayer structure is also calculated.[53] When VO_2 is in the metallic state, the real part of the equivalent impedance $\mathrm{Re}\,(Z)$ at 9.89 μm is close to 1.0, and the imaginary part $\mathrm{Im}\,(Z)$ is zero [Fig. 3(a)], which matches well with free space. The reflection loss is greatly reduced, thereby obtaining an ultra-high emissivity. On the other hand, when VO_2 is in the dielectric state, the impedance is mismatched in Fig. 3(b), which increases the reflection and leads to a lower emissivity.

Figure 4(a) explores the emissivity of the radiative cooler as a function of ambient temperature. The obtained emissivity can be well-tuned by the external thermal stimuli. At low temperature, the emissivity of the cooler remains at a low value. However, when the temperature approaches the phase transition temperature, the emissivity in the atmospheric window starts to increase and reaches a maximum when the phase transition is completed. The corresponding average emissivity at each temperature is presented in Fig. 4(b). It is only 3.8% at 273 K but starts to increase at 293 K, reaching a maximum value of 96.0% at 313 K, highlighting the temperature-responsive behavior of VO_2.

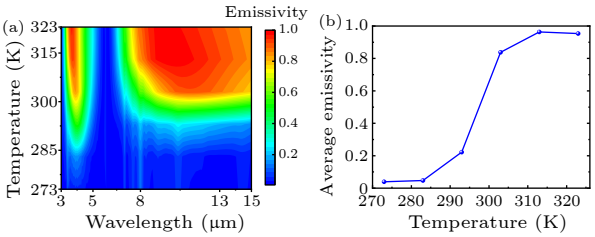

Fig. 4. (a) Emissivity of the radiative cooler at different temperatures. (b) The average emissivity at each temperature.

The thickness of the PVC layer can be effectively altered through external strain, providing us with another way to manipulate the optical response.[54] When a longitudinal force is applied to the PVC layer it will become thinner. The variation of the original thickness d_3 is denoted as Δd and the strain is defined as $\Delta d/d_3$.[22,55]

In our design, the optimal thickness of the PVC layer is 1 μm. Figure 5(a) demonstrates the required stain when the initial thickness of the PVC layer ranges from 2 μm to 6 μm. Specifically, when the thickness of the PVC layer is 6 μm, the emissivity spectrum of the cooler at zero strain is illustrated in Fig. 5(b). An average emissivity of 60.4% is obtained. However, by applying a strain of 34%, this value can be increased to 76.3%. The average emissivity of the cooler can be improved to 96.3% by applying a strain of 83% to achieve the optimal thickness. Therefore, the cooling performance of the emitter can be flexibly modulated by external strain to obtain the expected cooling temperature.[22]

Figure 6(a) examines the absorption of the adaptive radiative cooler in the solar band. Its average absorptivity is only 43.38%, which greatly offsets the cooling power and limits its application. In this regard, the top selective filter is included to minimize the impact of solar radiation and enable efficient daytime cooling. It consists of 11 layers of Si/KBr, and the thickness of each layer from top to bottom is specified in Table 1. The presence of the Si layer effectively blocks the downward-propagating sunlight.[52] Figure 6(b) illustrates the transmittance of the filter, which exhibits a low transmittance of 2.5% from

0.3 μm to 2.5 μm, and it can effectively block out solar radiation. Additionally, the filter possesses a selective transmittance of up to 96.7% in the wavelength range from 8 μm to 13 μm, thereby ensuring the efficient transmission of high emission from bottom of the radiative cooler.

Table 1. Thickness of the designed spectrally selective filter.

Layer	Material	Thickness (μm)
1	Si	0.26
2	KBr	0.50
3	Si	0.58
4	KBr	0.24
5	Si	0.18
6	KBr	1.14
7	Si	0.16
8	KBr	1.02
9	Si	0.66
10	KBr	0.52
11	Si	0.28

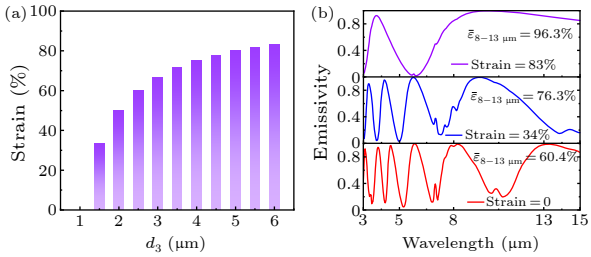

Fig. 5. (a) The strain required to obtain the optimal thickness in our design for different initial thicknesses of the PVC layer. (b) Emissivity spectrum of the cooler at different strains for a 6 μm PVC layer.

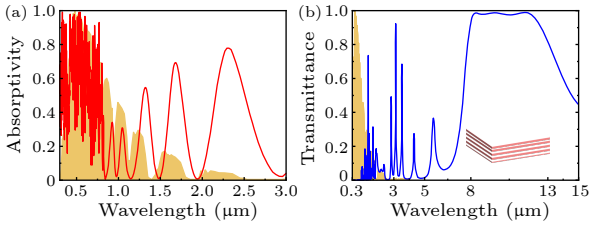

Fig. 6. (a) Absorptivity of the radiative cooler in the solar band when VO_2 is in the metallic state. (b) Transmittance of the filter in the solar band and atmospheric window. The inset shows a filter consisting of 11 layers of Si/KBr.

We employ the incoherent summation method to solve for the emissivity $\varepsilon(\lambda, \Omega)$ of the adaptive radiative cooling system as follows:[32,56]

$$\begin{aligned}\varepsilon(\lambda, \Omega) = &\ (1 - r_c)\left[t_F + t_F r_c t_F + t_F (r_c t_F)^2\right. \\ &\left. + t_F (r_c t_F)^3 + \cdots\right] \\ = &\ t_F (1 - r_c) / (1 - r_F r_c), \end{aligned} \tag{11}$$

where Ω stands for the solid angle, t_F is the power transmission coefficient of the top filter, r_F denotes the power reflection coefficient of the top filter, and r_c represents the power reflection coefficient of the bottom radiative cooler. The absorptivity and emissivity of the adaptive thermal emitter in the solar and atmospheric window bands are illustrated in Figs. 7(a) and 7(b), respectively. When the cooling function is activated at high temperature, the absorptivity in the solar band is only 1.6%, and the average emissivity in the atmospheric window is as high as 93.4%, indicating that the emitter is able to radiate heat away during the daytime. At low temperature, our design automatically deactivates cooling and the average emissivity of the transparent window drops to 3.8%, preventing heat loss. Hence, the adaptive radiative cooler we designed can efficiently cool and keep heat based on the ambient temperature without additional energy input. Additionally, if the filter is placed directly on the top of the cooler, the average emissivity at high and low temperatures is 3.0% and 88.9%, respectively. By comparison, the combined structure demonstrates a superior adaptive cooling performance when the filter and the cooler are separated.

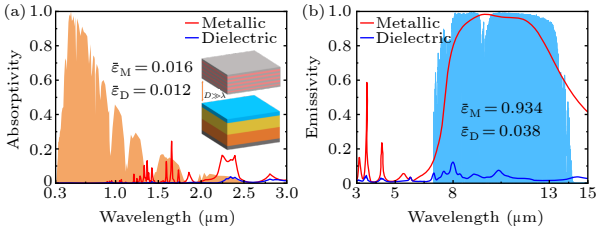

Fig. 7. Absorptivity of the adaptive radiative cooling emitter (a) in the solar band and (b) in the atmospheric transparent window.

In practice, it is important to evaluate the cooling performance of the adaptive emitter at different incidence angles.[57] Figures 8(a) and 8(b) exhibit the emissivity in the adaptive radiative cooler in both TE and TM polarization at high temperature, respectively. Broadband emission can be achieved in the atmospheric transparent window. Thus, the emitter exhibits excellent selective emission at different incident angles. The average emissivity remains above 90% when the incidence angle is less than 50° in Fig. 8(c). The emissivity partially decreases for angles larger than 50°, but still maintains in a high value. At an incident angle of 80°, the average emissivity is 78.4%. These results demonstrate that our designed adaptive radiative cooler is insensitive to variations of incident angle at high temperature and possesses superior cooling behavior.

The cooling power of the adaptive radiative cooler as a function of temperature is presented in Fig. 9(a) without considering the non-radiative heat transfer. The radiative cooling mode switches off when the surface temperature is 283 K. The corresponding absorbed solar radiation power P_{sun} is 16.39 $W \cdot m^{-2}$, which is larger than the radiative power P_{rad} (11.11 $W \cdot m^{-2}$), indicating that the cooling function of the adaptive emitter does not work at low temperature. On the other hand, when the surface temperature exceeds the phase transition temperature T_c, the growth of the atmospheric window emissivity leads to a sig-

nificant increase in cooling power, and activates the cooling mode. Specifically, the net daytime cooling power P_{daytime} is as high as 156.4 $\text{W}\cdot\text{m}^{-2}$ at an ambient temperature of 303 K, allowing for efficient cooling. Figure 9(b) considers the influence of the non-radiative heat transfer coefficient (h_c) on the net cooling power. At high temperature, a larger h_c enhances heat exchange between the environment and the adaptive radiative cooler, resulting in a gradual increase in the net cooling power, proving that the emitter is suitable for different environmental conditions.[58]

Table 2. Comparison of our VO_2-based adaptive thermal emitter with other works.

Structure	ε_{low}	$\varepsilon_{\text{high}}$	$\Delta\varepsilon$	Wave band (μm)	Reference
CaF_2/VO_2	0.47	0.83	0.36	4–12.5	[59]
VO_2/PMMA/ITO/Glass/ITO	0.21	0.61	0.4	8–14	[60]
(Filter)/VO_2/MgF_2/W	0.054	0.636	0.582	8–13	[28]
(Filter)/Ge/ VO_2/Ti	0.2	0.8693	0.6693	8–13	[24]
(Reflector)/PMMA/VO_2/Si/Ag	0.18	0.78	0.6	8–14	[25]
(Filter)/VO_2/HfO_2/Al	0.21	0.82	0.61	8–14	[52]
VO_2/Ge/VO_2/Ag	0.1	0.78	0.68	5–13	[31]
BaF_2/VO_2/ BaF_2/VO_2 $BaF_2/VO_2/BaF_2$/Al	0.28	0.95	0.67	5–22	[61]
VO_2/NaCl/PVC/Ag	0.037	0.963	0.926	8-13	our work
(Filter)/VO_2/NaCl/PVC/Ag	0.038	0.934	0.896	8–13	our work

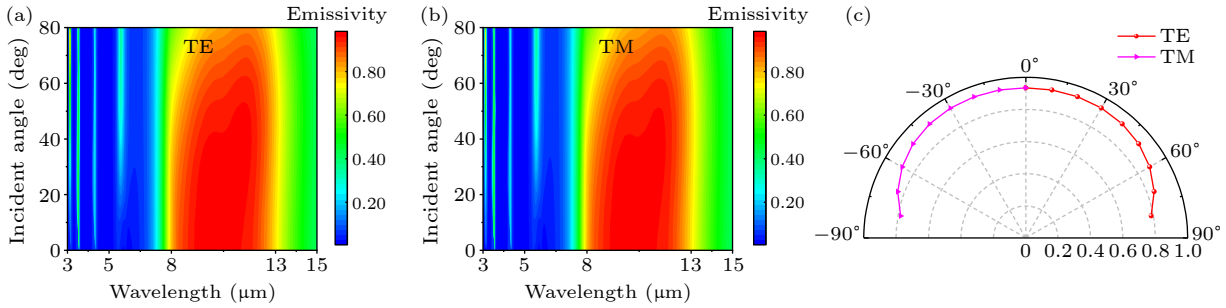

Fig. 8. Contour plots of the emissivity in the adaptive radiative cooler in (a) TE mode and (b) TM mode. (c) Average emissivity of the radiative cooler as a function of incident angle.

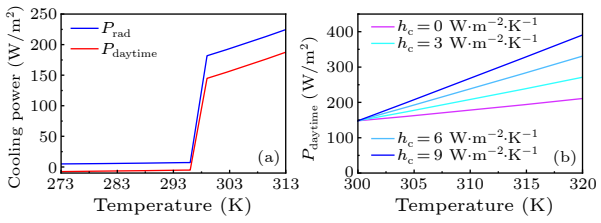

Fig. 9. (a) Radiative power P_{rad} and daytime net cooling power P_{daytime} for the designed adaptive radiative cooler. (b) Net cooling power at different convection coefficients when VO_2 is in the metallic states.

In comparison, we also list the differences in structural design, high and low-temperature emissivity, and working band range of VO_2-based adaptive thermal emitters in Table 2. Here ε_{low} and $\varepsilon_{\text{high}}$ stand for the emissivity of the adaptive radiative cooler at low and high temperature, respectively. $\Delta\varepsilon$ represents the modulation range of emissivity that can be calculated from $\varepsilon_{\text{low}} - \varepsilon_{\text{high}}$. Obviously, our designed adaptive radiative cooler possesses superior cooling performance, more stable emission behavior and a wider regulation range. Thus, our adaptive design is promising for energy conservation and environmental protection and it can be widely applied in buildings, spacecraft, vehicles, and other related areas.

In summary, we have developed an innovative adaptive radiative cooling emitter that comprises a filter and an FP cavity. The emitter activates radiative cooling at high temperature, with the emissivity of the atmospheric transparent window at 93.4%, and the daytime solar absorptivity as low as 1.6%, enabling efficient cooling. The cooling power is as high as 156.4 $\text{W}\cdot\text{m}^{-2}$ at an ambient temperature of 303 K. At low temperature, the emissivity rapidly decreases to 3.8%, and the cooling function is deactivated to prevent heat loss. The adaptive radiative cooling emitter automatically activates or deactivates radiative cooling according to the ambient temperature without requiring additional energy input. Additionally, the adaptive emitter demonstrates remarkable selective thermal emission even when the external stain, incident angle or heat transfer coefficient are varied. Therefore, this work significantly improves the cooling performance of adaptive radiative cooling devices and provides a reference for applications of thermotropic phase change materials in smart thermal management.

Acknowledgment. This work was supported by the Natural Science Foundation of Henan Province (Grant No. 232102231023).

References

[1] Liang J, Wu J, Guo J, Li H, Zhou X, Liang S, Qiu C W, and Tao G 2023 *Natl. Sci. Rev.* **10** nwac208

[2] Su W, Cai P, Darkwa J, Hu M, Kokogiannakis G, Xu C, and Wang L 2023 *Appl. Therm. Eng.* **235** 121305

[3] Chae D, Kim M, Jung P H, Son S, Seo J, Liu Y, Lee B J, and Lee H 2020 *ACS Appl. Mater. Interfaces* **12** 8073

[4] Raman A P, Anoma M A, Zhu L, Rephaeli E, and Fan S 2014 *Nature* **515** 540

[5] Fan S H and Li W 2022 *Nat. Photon.* **16** 182

[6] Liu Y N, Weng X L, Zhang P, Li W X, Gong Y, Zhang L, Han T C, Zhou P H, and Deng L J 2021 *Chin. Phys. Lett.* **38** 034201

[7] Li X G, Peoples J, Yao P, and Ruan X L 2021 *ACS Appl. Mater. Interfaces* **13** 21733

[8] Mandal J, Yang Y, Yu N F, and Raman A P 2020 *Joule* **4** 1350

[9] Zhai Y, Ma Y G, David S N, Zhao D, Lou R, Tan G, Yang R, and Yin X 2017 *Science* **355** 1062

[10] Li J L, Liang Y, Li W, Xu N, Zhu B, Wu Z, Wang X Y, Fan S H, Wang M H, and Zhu J 2022 *Sci. Adv.* **8** eabj9756

[11] Mandal J, Fu Y K, Overvig A C, Jia M X, Sun K R, Shi N N, Zhou H, Xiao X H, Yu N F, and Yang Y 2018 *Science* **362** 315

[12] Liu J W, Tang H J, Jiang C X, Wu S Q, Ye L, Zhao D L, and Zhou Z H 2022 *Adv. Funct. Mater.* **32** 2206962

[13] Xia H, Yin H Y, and Fan C Z 2023 *J. Quant. Spectrosc. Radiat. Transfer* **306** 108659

[14] Yin H Y and Fan C Z 2023 *Results Phys.* **45** 106216

[15] Yin H Y and Fan C Z 2023 *Chin. Phys. Lett.* **40** 077801

[16] Yang F B, Zhang Z R, Xu L J, Liu Z F, Jin P, Zhuang P F, Lei M, Liu J R, Jiang J H, Ouyang X, Marchesoni F, and Huang J P 2024 *Rev. Mod. Phys.* **96** 015002

[17] Zhang C X, Li T J, Xu L J, and Huang J P 2023 *Chin. Phys. Lett.* **40** 054401

[18] Wang J Y, Tan G, Yang R G, and Zhao D L 2022 *Cell Rep. Phys. Sci.* **3** 101198

[19] Zhang L P, Wang B, Li X B, Xu G P, Dou S L, Zhang X, Chen X, Zhao J P, Zhang K, and Li Y 2019 *J. Mater. Chem. C* **7** 9878

[20] Xia Z L, Fang Z, Zhang Z F, Shi K L, and Meng Z H 2020 *ACS Appl. Mater. Interfaces* **12** 27241

[21] Mandal J, Jia M X, Overvig A, Fu Y K, Che E, Yu N F, and Yang Y 2019 *Joule* **3** 3088

[22] Liu Y, Tian Y P, Liu X J, Chen F Q, Caratenuto A, and Zheng Y 2022 *Appl. Phys. Lett.* **120** 171704

[23] Xu J Y, Chen D, and Meng S 2022 *Sci. Adv.* **8** eadd2392

[24] Zhang W W, Qi H, Sun A T, Ren Y T, and Shi J W 2020 *Opt. Express* **28** 20609

[25] Kim M, Lee D, Yang Y, and Rho J 2021 *Opto-Electron. Adv.* **4** 200006

[26] Zhang D R, Wu B Y, Liu H T, Yang B, Sun Y S, and Wu X H 2023 *Int. J. Therm. Sci.* **185** 108039

[27] Jia Y L, Wang X X, Yin H Y, Yao H W, Wang J Q, and Fan C Z 2021 *Appl. Opt.* **60** 5699

[28] Ono M, Chen K F, Li W, and Fan S H 2018 *Opt. Express* **26** A777

[29] Tang K C, Dong K C, Li J C, Gordon M P, Reichertz F G, Kim H, Rho Y, Wang Q, Lin C Y, Grigoropoulos C P, Javey A, Urban J J, Yao J, Levinson R, and Wu J 2021 *Science* **374** 1504

[30] Xie B W, Zhang W J, Zhao J M, Zheng C, and Liu L H 2024 *Appl. Therm. Eng.* **236** 121751

[31] Liang S R, Xu F, Li W X, Yang W X, Cheng S B, Yang H, Chen J, Yi Z, and Jiang P P 2023 *Appl. Therm. Eng.* **232** 121074

[32] Li B, Hu J, Chen C, Hu H, Zhong Y, Song R, Cao B, Peng Y, Xia X, Chen K, and Xia Z 2024 *Nanophotonics* **13** 725

[33] Huang J C, Zhang X K, Yu X, Tang G H, Wang X Y, and Du M 2024 *Renew. Energ.* **224** 120208

[34] Bhupathi S, Wang S C, Wang G Y, and Long Y 2024 *Nanophotonics* **13** 711

[35] Heavens O S 1992 *J. Mod. Opt.* **39** 189

[36] Mandal P, Speck A, Ko C, and Ramanathan S 2011 *Opt. Lett.* **36** 1927

[37] Jepsen P U, Fischer B M, Thoman A, Helm H, Suh J Y, Lopez R, and Haglund R F 2006 *Phys. Rev. B* **74** 205103

[38] Smith N V 2001 *Phys. Rev. B* **64** 155106

[39] Wang H, Yang Y, and Wang L 2014 *J. Appl. Phys.* **116** 123503

[40] Barker A S, Verleur H W, and Guggenheim H J 1966 *Phys. Rev. Lett.* **17** 1286

[41] Dickinson E J F, Ekström H, and Fontes E 2014 *Electrochem. Commun.* **40** 71

[42] Musil J, Čiperová Z, Čerstvý R, and Haviar S 2019 *Thin Solid Films* **688** 137216

[43] Shah D, Patel D I, Roychowdhury T, Johnson B I, and Linford M R 2020 *Appl. Surf. Sci.* **526** 146621

[44] Ao X Z, Li B W, Zhao B, Hu M K, Ren H, Yang H L, Liu J, Cao J Y, Feng J S, Yang Y J, Qi Z M, Li L B, Zou C W, and Pei G 2022 *Proc. Natl. Acad. Sci. USA* **119** e2120557119

[45] Xie H L, Yin H Y, Xia H, and Fan C Z 2024 *Int. J. Heat Mass Transfer* **222** 125176

[46] Liu J W, Zhang Y F, Li S, Valenzuela C, Shi S K, Jiang C X, Wu S Q, Ye L, Wang L, and Zhou Z H 2023 *Chem. Eng. J.* **453** 139739

[47] Han D, Ng B F, and Wan M P 2020 *Sol. Energy Mater. Sol. Cells* **206** 110270

[48] Xu L J, Yang S, Dai G L, and Huang J P 2020 *ES Energy Environ.* **7** 65

[49] Yin H Y, Yao H W, Jia Y L, Wang J Q, and Fan C Z 2021 *J. Phys. D* **54** 345501

[50] Yao H W, Wang X X, Yin H Y, Jia Y L, Gao Y, Wang J Q, and Fan C Z 2021 *Chin. Phys. B* **30** 064214

[51] Jayamaha S E G, Wijeysundera N E, and Chou S K 1996 *Build. Environ.* **31** 399

[52] Xu X D, Gu J X, Zhao H P, Zhang X Y, Dou S L, Li Y, Zhao J P, Zhan Y H, and Li X F 2022 *ACS Appl. Mater. Interfaces* **14** 14313

[53] Fan C Z, Xie H L, and Wang J H 2023 *Sol. Energy* **266** 112192

[54] Ying J W, Huang J Z, Qin S K, and Huang Y J 2021 *Appl. Sci.* **11** 6830

[55] Butler A and Argyropoulos C 2022 *Appl. Therm. Eng.* **211** 118527

[56] Large M C J, Mckenzie D R, and Large M I 1996 *Opt. Commun.* **128** 307

[57] Wang K, Luo G, Guo X, Li S, Liu Z, and Yang C 2021 *Sol. Energy* **225** 245

[58] Zhao B, Hu M, Ao X, Chen N, and Pei G 2019 *Appl. Energy* **236** 489

[59] Wu X Y, Yuan L, Weng X L, Qi L, Wei B, and He W T 2021 *Nano Lett.* **21** 3908

[60] Wang S C, Jiang T Y, Meng Y, Yang R G, Tan G, and Long Y 2021 *Science* **374** 1501

[61] Xie B W, Zhang W J, Zhao J M, and Liu L H 2022 *Opt. Express* **30** 34314